Northumbria Research Link

Citation: Zhou, Jian, Zhang, Dinghong, Liu, Yanghui, Zhuo, Fengling, Qian, Lirong, Li, Honglang, Fu, Yong Qing and Duan, Huigao (2022) Record-breaking Frequency of 44 GHz Based on Higher Order Mode of Surface Acoustic Waves with LiNbO3/SiO2/SiC Heterostructures. Engineering. ISSN 2095-8099 (In Press)

Published by: Elsevier

URL: https://doi.org/10.1016/j.eng.2022.05.003 <https://doi.org/10.1016/j.eng.2022.05.003>

This version was downloaded from Northumbria Research Link: http://nrl.northumbria.ac.uk/id/eprint/49077/

Northumbria University has developed Northumbria Research Link (NRL) to enable users to access the University's research output. Copyright © and moral rights for items on NRL are retained by the individual author(s) and/or other copyright owners. Single copies of full items can be reproduced, displayed or performed, and given to third parties in any format or medium for personal research or study, educational, or not-for-profit purposes without prior permission or charge, provided the authors, title and full bibliographic details are given, as well as a hyperlink and/or URL to the original metadata page. The content must not be changed in any way. Full items must not be sold commercially in any format or medium without formal permission of the copyright holder. The full policy is available online: http://nrl.northumbria.ac.uk/policies.html

This document may differ from the final, published version of the research and has been made available online in accordance with publisher policies. To read and/or cite from the published version of the research, please visit the publisher's website (a subscription may be required.)

Northumbria University NEWCASTLE

University Library

Record-breaking Frequency of 44 GHz Based on Higher Order Mode of Surface Acoustic Waves with $LiNbO_3/SiO_2/SiC$ Heterostructures

Jian Zhou[1], Dinghong Zhang[1], Yanghui Liu[1], Fengling Zhuo[1], Lirong Qian[2,*], Honglang Li[3], Yong-Qing Fu[4], Huigao Duan[1,*]

1. College of Mechanical and Vehicle Engineering, Hunan University, Changsha 410082, China
2. Tianjin Key Laboratory of Film Electronic and Communicate Devices, School of Integrated Circuit Science and Engineering, Tianjin University of Technology, Tianjin 30084, PR China
3. CAS Center for Excellence in Nanoscience, National Center for Nanoscience and Technology, Beijing 100190, China
4. Faculty of Engineering and Environment, Northumbria University, Newcastle upon Tyne, NE1 8ST, United Kingdom

Corresponding Email: duanhg@hnu.edu.cn; lirongqian83@email.tjut.edu.cn

Abstract: Surface acoustic wave (SAW) technology has been extensively explored for wireless communication, sensors, microfluidics, photonics and quantum information processing. However, due to their fabrication issues, SAW devices' frequencies are typically limited within a few GHz, which severely restricts their applications in 5G communication, precision sensing, photonics and quantum control. To solve this critical problem, we proposed a hybrid strategy which integrates extreme-nanomanufacturing process (e.g., nanolithography) and $LiNbO_3/SiO_2/SiC$ heterostructure structure, and successfully achieved a record-breaking frequency ~44 GHz of SAW devices and large electromechanical coupling coefficients up to 15.7%. We performed theoretical analysis and identified the guided higher-order wave modes generated on these slow-on-fast SAW platforms. To demonstrate its superior sensing performance, we have performed micro-mass sensing, and obtained an extremely high sensitivity of ~33151.9 MHz×mm^2/μg, which is ~10^{11} times higher than that of a conventional quartz crystal microbalance (QCM) and ~4000 times higher than that of a conventional SAW device with a frequency of 978 MHz.

Keywords: ultra-high frequency; SAW; higher-order-mode; hypersensitive detection

1. Introduction

Surface acoustic wave (SAW) technology is currently extensively applied for applications in physical and biochemical sensors [1], photonics [2] and quantum acoustics, communication, signal processing [3] and lab-on-a-chip [4]. The maximum working frequencies of many conventional SAW devices are up to a few gigahertz (GHz), which cannot meet the strong demands of ultrahigh frequency acoustic wave devices for future electronics and communications. It is critically required for the SAW devices to be operated at higher frequencies (>3 GHz) for precision sensing [5], 5G communication, and quantum control of SAW induced phonons [6], as well as integrated microwave-photonics signal processing [7].

A SAW device's resonant frequency, f, is linked with the acoustic wave velocity v and the

wavelength (λ), based on the formula of $f=v/\lambda$. To increase the SAW device's frequency, two main methods are frequently used. The mostly common approach is to reduce the value of λ *via* increasing the resolution of patterns using a nanoscale manufacturing technology [8]. In Ref [9], Büyükköse et al. reported that a SAW device based on $ZnO/SiO_2/Si$ structure achieved a high frequency of 16.1 GHz using a nanoimprint lithography [9]. Using an electron beam lithography (EBL), Mohammad *et al.* achieved a high frequency of 14.2 GHz for a $LiNbO_3$ SAW device with a wavelength of 200 nm [10]. Our group has recently reported a $LiNbO_3$ SAW device with a 30 GHz frequency, which was made using an improved EBL process [11]. The second approach is to design and apply slow-on-fast structures by using a film with a low velocity on top of a substrate, which has a much higher value of acoustic velocity, e.g., ZnO/SiC [12], AlN/SiC [13], ZnO/diamond [14], AlN/diamond [15], AlN/Pt/diamond/Si [16]. Previously, our group has reported that high frequencies of 33.7 GHz [17] and 17.7 GHz [18] have been successfully obtained with the SAW devices based on AlScN/diamond/Si and AlN/diamond/Si structures, using the EBL technology.

However, there are several key issues which need to be solved. (1) To reduce the value of λ, most of researchers focus on pushing the dimensions limits of the interdigital transducers (IDTs) on a single crystal substrate, such as $LiNbO_3$, due to its excellent surface smoothness and high electromechanical coupling coefficient (K^2). However, these single crystal substrates often have low wave velocities and/or are incompatible with complementary metal oxide semiconductor (CMOS) process. (2) For the slow-on-fast structure designs, the piezoelectric materials are normally ZnO or AlN which have relatively low K^2 values, and thus severely affect the device's performance. Recently, single crystal film/SiC based SAW devices on multilayered substrates of $LiNbO_3$/SiC [19] or $LiNbO_3/SiO_2$/SiC [20] were utilized for making high frequency SAW devices, especially for SAW filters. However, previous studies are mainly focused on SAW devices with working frequencies lower than 5 GHz, without much focusing on the potentially generated multiple acoustic modes for superhigh frequency applications.

To address these critical issues, herein, we proposed a hybrid strategy which integrates nanoscale extreme manufacturing processes and heterostructures design on slow-on-fast substrates, and successfully break the frequency record of the current SAW devices. Based on this novel idea, we developed heterostructures of $LiNbO_3/SiO_2$/SiC, and applied an electron beam lithography with a proximity effect correction (PEC) algorithm to optimize the dimensions of SAW IDTs, which can achieve a finger width of electrode down to 35 nm. Finite element method (FEM) was applied to theoretically analyze and identify the higher-order acoustic modes of $LiNbO_3$ films based slow-on-fast SAW devices. We then successfully fabricated the SAW devices with frequencies from 5 to ~44 GHz. Finally, a super-high mass sensitivity was achieved, demonstrating its superior sensing performance and potential applications for such a high frequency SAW platform.

2. Experimental

Figure 1a illustrates the overall structure of the proposed one-port ultra-high frequency SAW resonator, which is manufactured on a $LiNbO_3/SiO_2$/SiC multilayered heterostructure. A 4-inch X cut-34°Y $LiNbO_3$ single crystal was applied as the piezoelectric layer due to its relatively high value of K^2 and excellent surface smoothness which are beneficial for device fabrication and performance. The detailed fabrication processes of $LiNbO_3$ single crystal film

on the slow-on-fast substrates are shown in Figure S1, which is based on a typical ion-cut process. SiC was applied as the carrier substrate because it exhibits large velocities for both shear waves (7100 m/s) and longitudinal waves (12,500 m/s) [21], low propagation loss and high thermal conductivity. As it is well-known, SiC is one of the third-generation semiconductor materials with the capability for integration of microelectronic devices with the SAW devices on one single chip [22]. In this multilayer design, SiO_2 was applied as a temperature compensation layer. Figure S2 presents the technological process diagram of the EBL and lift-off for patterning the nanoscale IDTs. The optimized PEC algorithm for the EBL has previously been reported in Ref. [11]. In this work, wavelengths from 160 to 800 nm were prepared. The IDTs have a pair number of 50, and the aperture (L) is 20 λ. The reflectors are separated from the IDTs with a distance of 0.25 λ. The detail geometrical information of the SAW devices is summarized in Table S1.

The fabricated structures of IDTs and cross-section morphology of the $LiNbO_3/SiO_2/SiC$ multilayer were checked using a scanning electron microscope (SEM, Carl-Zeiss Sigma HD, Germany). An X-ray diffractometer (XRD, D8 ADVANCE, Germany) was used to characterize the crystalline structures of the films. Surface topography of the $LiNbO_3$ film/SiO_2/SiC multilayer was investigated using an atomic force microscope (AFM, SPI-3800N, Seiko Co. Japan). Device performance was characterized using an R&S®ZVA vector network analyzer (with its maximum frequency up to 67 GHz), together with MPI 200 mm automated engineering probe system (MPI TS2000-SE) and ground-signal-ground (GSG) probes. Before the scatter (S)-parameter measurements of fabricated SAW devices, we used the calibration chips for the difference cases of open circuit, short circuit and load calibration, in order to minimize the parasitic parameters generated by the radio frequency cable and probe test equipment.

The sensing mechanism of mass detection was based on the loading effect of the gold (Au) IDT electrodes, which was reported in our previous work [23]. Different Au IDT thicknesses of 20 nm (defined as 0 mass loading) and 25 nm (with an estimated mass-loading of 0.0966 $\mu g \cdot mm^{-2}$) were employed as different mass loadings on the SAW device, and then the changes of frequency signals were obtained. In this study, Au was selected as the material for IDT electrodes, as it shows a better electrical conductivity than aluminum, and during the lift-off process, it shows less defect formation and failure of the IDTs.

Temperature effects on the responses of SAW devices were studied using a probe system and a network analyzer with a LabVIEW program. The MPI probe system has an integrated thermal chuck (20~300°C), with a touchscreen display, placed conveniently in front of the operator for fast operations and immediate feedbacks. The SAW samples were placed on a loading chuck of the probe system during the test, and the GSG probe was used to connect the SAW IDTs with the network analyzer. We used the touchscreen display to adjust the temperature and heated the loading chuck inside the equipment to adjust the temperature to the set point, and then recorded the changes of the frequency signals.

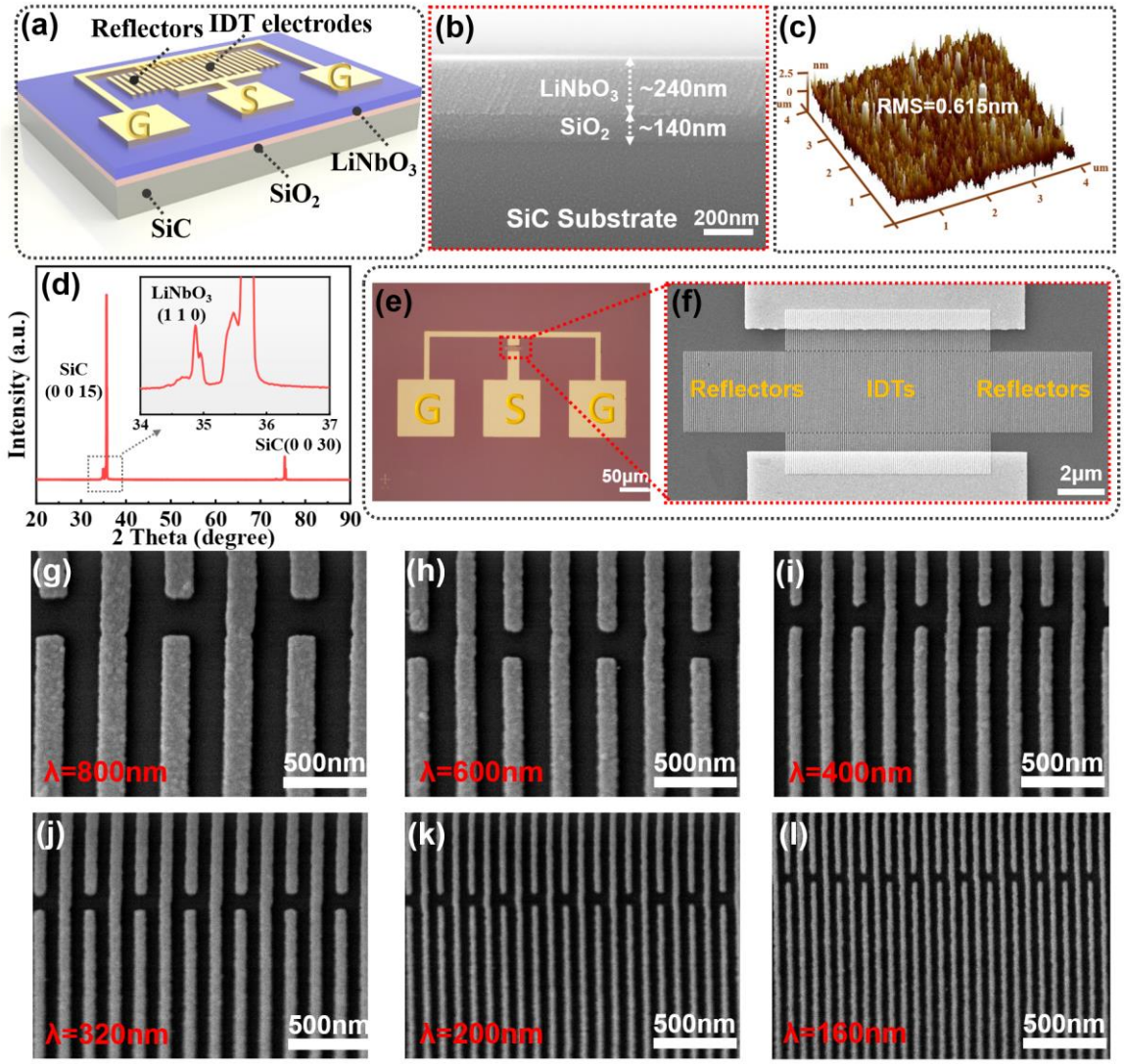

Figure 1. (a) Schematic illustration of the proposed one-port SAW device using the $LiNbO_3/SiO_2/SiC$ heterostructure; (b) Cross-section morphology of $LiNbO_3/SiO_2/SiC$ heterostructure; (c) AFM micrograph of the $LiNbO_3/SiO_2/SiC$ substrate; (d) XRD pattern of $LiNbO_3/SiO_2/SiC$ substrate. (e) Optical image of fabricated SAW with a λ of 160 nm; (f) ~ (i) SEM images of IDTs with number of both IDT pairs and reflectors of 50, and different λ of 800, 600, 400, 320, 200 and 160 nm.

3. Results and discussion

Figure 1b presents an SEM image of the SAW device based on the $LiNbO_3/SiO_2/SiC$ heterostructure. Results showed that the single crystalline $LiNbO_3$ films are seamlessly bonded onto the SiO_2/SiC substrate. The thicknesses of $LiNbO_3$ film and SiO_2 film are ~220 nm and ~140 nm on the SiC carrier substrate. Figure 1c shows an AFM image, revealing the surface morphology of the SAW device. The roughness value of the $LiNbO_3$ film is about 0.615 nm (a root mean square or RMS value), and it is much smaller than those of AlN or ZnO film based slow-on-fast substrates reported in literature [12-16]. The smooth surface is vital to push the limit of frequency by reducing IDT finger width *via* improved patterning resolution using the extreme nano-manufacturing technology. Figure 1d shows XRD spectra of $LiNbO_3$ film on the SiC substrate. There is only one peak at two theta angle of ~34°, exhibiting the highly oriented

(110) $LiNbO_3$ film. Figure 1e is the optical image of SAW device. Figure 1f presents the complete IDTs, demonstrating that our optimized manufacturing method using the improved EBL can successfully achieve nanoscale patterns of IDTs. Figures 1g~l present a series of SEM images of SAW IDTs with wavelength λ of 160, 200, 320, 400, 600 and 800 nm. Clearly an ultra-high resolution IDT finger with a 160 nm wavelength and a width of ~35 nm (Figure S3) was realized. Through a thorough literature survey, we have confirmed that this value is the smallest wavelength for all the slow-on-fast layer structure of SAW devices reported.

Admittance (Y_{11}) curves of the various fabricated devices are shown in Figure 2, and the reflectance (S_{11}) signals of the fabricated SAW devices are presented in Figure S4. Multiple acoustic modes can be observed for all the SAW samples. The range of resonant frequency is increased from 4 ~15 GHz to 10~42 GHz, as the wavelength is decreased from 800 nm to 160 nm. The signal amplitude is decreased slightly with the decrease of wavelength, which is attributed to the increased impedance of the devices with much finer IDT patterns. In addition, it is quite difficult to obtain the uniform IDT fingers for smaller wavelength devices, thus resulting in relative weak signals. Nevertheless, a high frequency value of ~41.5 GHz was recorded for the fabricated device with a wavelength λ of 160 nm. We have further fabricated four SAW samples with the same λ of 160 nm to verify that the high frequency obtained is not because of parasitic responses or noises. All these devices display similar results, as shown in Fig. S5, proving that this frequency signal is induced by SAWs.

To verify the modes of these multiple peaks, we have conducted numerical analysis using FEM method (with COMSOL software), and obtained admittance values of these SAW devices with different wavelengths. Figure 2 presents the obtained analysis results, which indicate that the simulated frequency signals of samples with various wavelengths are in good agreements with the experimental results. The detailed theoretical analysis and experimentally obtained results of SAW devices' frequencies can be seen in the supporting materials.

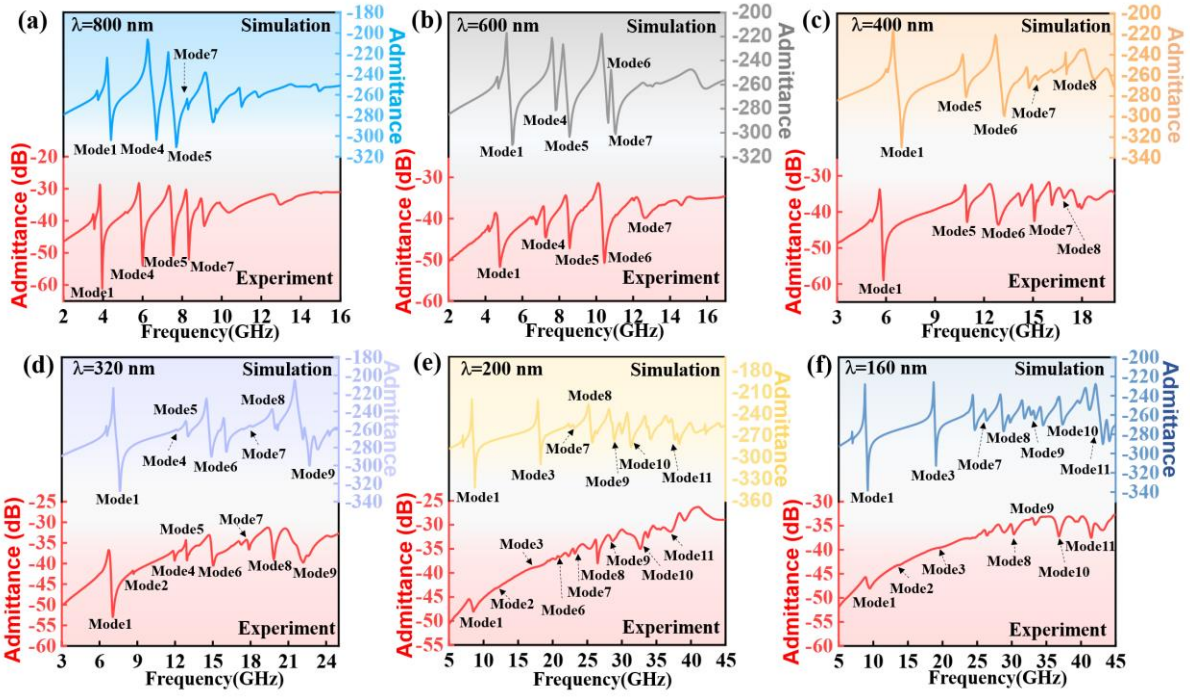

Figure 2. Admittance and resonant frequency performance spectra for the SAW samples with different λ of 800, 600, 400, 320, 200 and 160 nm, where the red line is the admittance of experimental SAW devices and

the upper line is the admittance characteristic of FEM simulation.

To further confirm the multiple modes of these SAW devices, eigenfrequency analysis was conducted to investigate the particle vibration patterns. Figure 3a presents the particle vibration pattern of each mode for the ultra-high frequency SAW devices. Clearly Mode 1 corresponds to shear-horizontal (SH) wave mode, and its particle displacements and wave vibrations are mainly existed along the direction of horizontal aperture [20], as shown in Fig. S6a. The Mode 2 is the standard Rayleigh wave [11], the Mode 3 is a longitudinal SAW coupled with harmonic metal thickness mode [24], the Mode 4 is longitudinal SAW [25], and the Mode 5 is high-order SH mode. All the other modes are the high-order SAWs which propagate near the SiC substrate [26]. It should be noted that with the decrease of SAW wavelength, more acoustic modes are excited and detected as illustrated in the Figure 3a. This is mainly due to the layered structure of SAW devices, the submicron thickness of the piezoelectric film, and the enhanced interference effect with the decrease of SAW wavelength. For example, as shown in Fig. 3a, only the Rayleigh mode (Mode 2) is observed if the wavelength is smaller than 320 nm. Whereas the Mode 10 and Mode 11 have been detected only when the wavelength is below 200 nm. These clearly shows that more higher-order SAW modes are generated when the wavelength is smaller than thickness of the layer [27].

The phase velocities of different wave modes as a function of the normalized thickness kH ($2\pi H/\lambda$, where H is the thickness of $LiNbO_3$ and k is the wave vector) are summarized in Fig. 3b. It is clear that with the increase of kH, the phase velocities of all these modes decrease, mainly because more acoustic energy is confined inside the $LiNbO_3$ layer whose sound velocity is much smaller that of the substrate.

Bode quality factors (Q) [28] of the SAW resonators with varied wavelengths can be calculated using:

$$Q = \frac{\omega \mid S_{11} \mid delay(S_{11})}{1 - \mid S_{11} \mid^2} \tag{1}$$

where delay (S_{11}) is group delay of the S_{11} parameters and ω is angular frequency. The measured Bode-Q curves of devices with different wavelengths are shown in Fig. S7. Table S2 and Fig. 3c summarize the calculated Q values for the SAW resonators with different wavelengths. With the increase of SAW wavelength, the Q value of each mode increases as shown in Fig. 3c, except for the modes 10 and 11. The reason for the decreased Q values for these smaller wavelength cases can be explained by the larger impedance values of the SAW devices with extremely narrow IDT fingers, higher acoustic loss, and also the non-uniformity of IDT widths produced by the nanoscale fabrication. The higher order modes of 10 and 11 are generated only for the IDT wavelengths of 200 and 160 nm. This is because the interference effect generated by the wave reflection from the SiC substrate is significantly enhanced when λ is smaller than the thickness of $LiNbO_3$ [27], thus a smaller wavelength is beneficial for the generation of higher modes for the ultra-high frequency SAWs [18]. The Q values of both mode 10 and mode 11 increase when the SAW devices' wavelength is decreased (from 200 nm to 160 nm), because of the increased interference effect of reflected acoustic waves from the substrate.

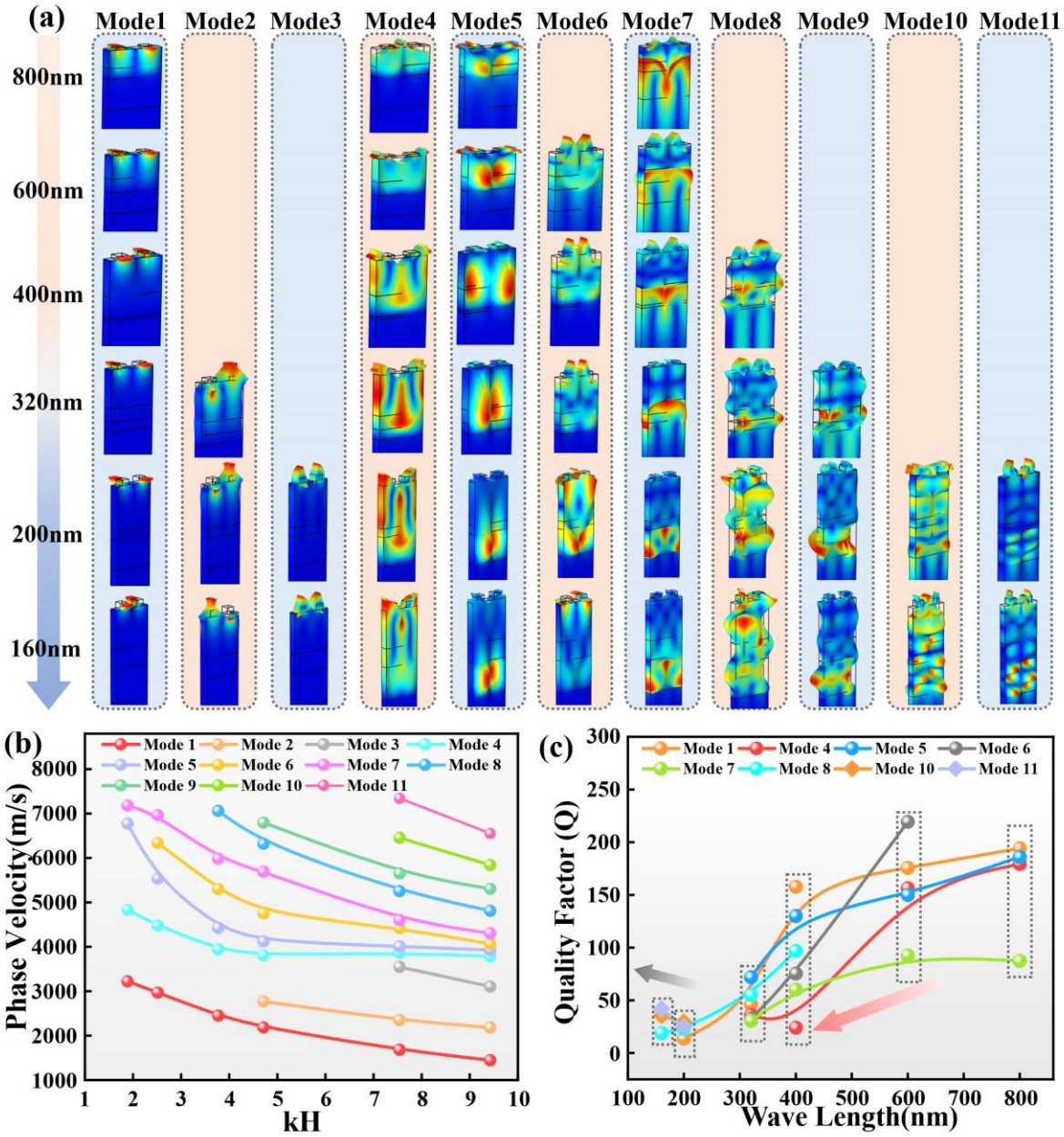

Figure 3. (a) Particle displacements of the multiple modes for the SAW with wavelength from 800 to 160 nm. (b) Phase velocity vs. the normalized film thickness on the $LiNbO_3/SiO_2/SiC$ structure (kH) SAW, where H represents $LiNbO_3$ thickness. (c) Q values vs. wavelengths for SAW with the λ from 800 to 160 nm.

The effective coupling coefficient (k^2_{eff}) can be calculated using:

$$k^2_{eff} = \frac{(\pi/2)\cdot(f_s/f_p)}{\tan((\pi/2)\cdot(f_s/f_p))} \quad (2)$$

where f_p and f_s are anti-resonant and resonant frequencies of admittance curves for the SAW resonators, respectively. Table S3 summarizes the obtained k^2_{eff} values of all the SAW devices. Results show that the Mode 1 (SH wave) has a higher k^2_{eff} value, compared with those of the other higher modes, which is consistent with theoretical simulations (Table S3). A high value of k^2_{eff} 15.7 % is obtained for the device with a frequency of ~10 GHz (SH wave) and the

wavelength of 160 nm. Whereas for the device with a frequency of 41.5 GHz (Mode 11), at the same wavelength of 160 nm, the k^2_{eff} value becomes 7.3 %. A detailed analysis of the SH mode which has relatively good performance and a large k^2_{eff} has been summarized in Fig. S6 in the supplementary materials.

For the demonstration of the application of these ultra-high frequency SAW devices, we have conducted mass detection tests by mass-loading onto the IDTs of the SAW devices [23]. Two different IDT thicknesses, e.g., 20 nm (which is assigned as the original state without any mass loading) and 25 nm (corresponding to a mass loading of 0.0966 μg·mm^{-2} on IDTs) for SAW devices were fabricated. Figures 4a and 4b as well as Fig. S8 show the mass sensing results using the fabricated SAW samples with wavelength λ of 320, 200, and 160 nm. With adding mass onto the IDTs, the frequency value of the SAW device is decreased for all these wavelengths. The SAW device's sensitivity can be calculated based on the changes of frequency divided by mass changes per sensing area [29], using the following formula:

$$S=\Delta f/(\Delta m/A) \quad (3)$$

where Δf is shift of the frequency, Δm is mass loading, S is the mass sensitivity, and A is the sensitive area. Table S4 summarizes the obtained mass sensitivity values of all the modes for the samples with various wavelengths. Results show that the devices with smaller wavelengths have much larger mass sensitivities, because of their higher working frequencies. As shown in Figure 4c, as the device's wavelength is decreased from 320 nm to 160 nm, its shift of frequency is increased from 648.9 MHz to 1527.9 MHz. These indicate the dramatically increased mass sensitivity values for the SH modes, e.g., 6717.1, 10183.9, and 15817.5 MHz·mm^2/μg, for the wavelengths of 320, 200, and 160 nm, respectively.

For a fixed wavelength, different modes have different sensitivity values. As shown in Figure 4c, the frequency shifts for the SH wave mode and Rayleigh wave mode are quite different under the same mass loading for all the wavelengths. Although the SH wave mode has a lower frequency, but its sensitivity is much higher compared with that of Rayleigh wave. This is because that SH wave's velocity is more sensitive to the mass loading on the electrode, especially for heavy metal films [30].

We have calculated all the mass sensitivity values for the SAW devices (Table S4), and the results show that the Mode 11 possesses much higher sensitivity values compared with those of the other modes. The highest mass-sensitivity for all the SAW devices is ~33151.9 MHz·mm^2/μg for the Mode 11 with the frequency of 44.2 GHz. Based on the extensive literature search, this frequency value is the highest reported frequency value for a SAW device. Compared with the mass sensitivity results of a conventional quartz crystal microbalance (QCM) and a standard SAW device with a frequency of 978 MHz reported in literature listed in Table 1, the corresponding value of our SAW device obtained in this study is about 10^{11} times higher, and ~4000 times higher, respectively.

The temperature characteristics of SAW devices is another important parameter for application. The temperature coefficient of frequency (TCF) of a SAW device can be calculated using:

$$TCF = \frac{1}{f_0}\frac{\Delta f}{\Delta T}\times 10^6 [\,ppm/K\,] \quad (4)$$

where, f_0 is the SAW device's resonant frequency at room temperature, Δf is the change of

frequency, ΔT is the temperature shift. For the $LiNbO_3/SiO_2/SiC$ based SAWs with wavelengths λ of 160 nm and 200 nm, the obtained TCF values are summarized in Fig. 4d and Fig. S9. As the SH wave mode has the best performance, and Mode 11 have the higher sensitivity values, we only show the TCF results of these two modes. The results clearly reveal a linear trend of frequency shift as a function of temperature as shown in Figure 4d. The TCF values are -165.8 ppm/K and -229.0 ppm/ K for the SH modes, and they are ~ -48.6 ppm/K and ~ -55.2 ppm/ K for the Mode 11, indicating that the Mode 11 is slightly less sensitive to temperature changes. In order to verify the TCF values, which we measured in the experiments, we theoretical calculated the temperature effects of the SH mode for SAW devices with λ of 160 nm. The obtained TCF value is ~154.4 ppm/K (Fig. S10), which is close to the experimentally obtained result (-165.8 ppm/ K).

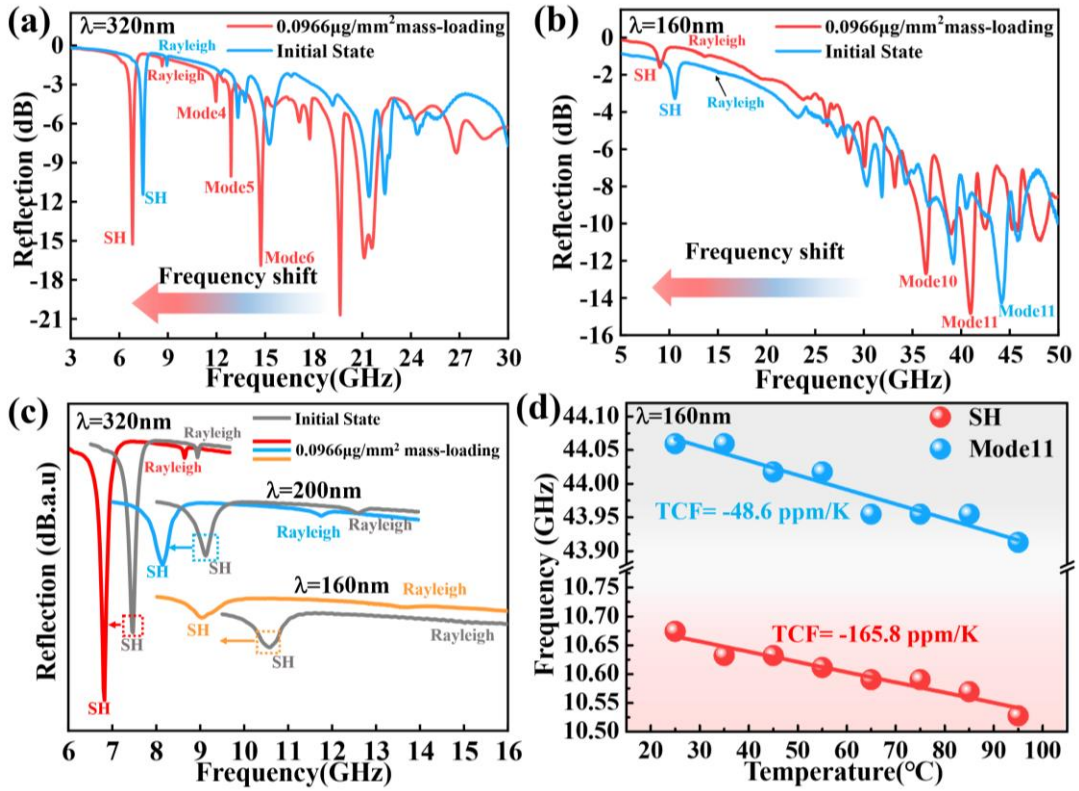

Figure 4. Frequency shift of the fabricated SAW device with λ of (a) 320 nm and (b) 160 nm with a mass loading of 0.0966 μg·mm^{-2} on IDTs. (c) Frequency responses of the SH and Rayleigh modes for the λ from 320 to 160 nm with a mass loading of 0.0966 μg·mm^{-2} on IDTs. (d) Resonant frequency shift of a device with λ of 160 nm vs. the temperature for the SH and Mode 11.

TABLE 1. Comparisons of mass sensitivity for SAW and QCM devices

Reference	*Year*	*Sensor*	*Working frequency(GHz)*	*Mass sensitivity*
[31]	2010	SAW	0.978	8.23 MHz×mm^2/μg
[32]	2016	SAW	0.385	155.8 KHz/μg
[33]	2017	SAW	0.122	9 KHz/μg
[34]	2017	QCM	0.01	1573 Hz/μg
[35]	2018	QCM	0.01	7940 Hz/μg
[36]	2020	QCM	0.01	1346 Hz/μg
This work	2021	SAW sensor	44.2	33151.915 MHz×mm^2/μg (2.6×10^{6}GHz/μg)

4. Conclusion

In this paper, we proposed a hybrid strategy to integrate extreme nano-manufacturing process with a heterostructure (slow-on-fast) design of $LiNbO_3/SiO_2/SiC$ to increase the frequency of the SAW device. We demonstrated that SAW devices with frequencies of 5~44 GHz were obtained with large electromechanical coupling coefficients. The proposed $LiNbO_3/SiO_2/SiC$ heterostructures in this study present multiple modes, and we have performed theoretical analysis and identified these higher-order guided wave modes. Furthermore, we have systematically investigated the mass sensitivity characteristics of these modes, and found that the SH mode has the best SAW resonance characteristics and is very sensitive to the mass-loading, indicating that it has great potentials for the high frequency sensing application. The Mode 11 possesses a much higher sensitivity value compared with those of the other modes and shows a relatively low TCF value. An ultrahigh mass sensitivity of ~33151.9 MHz×mm^2/μg was achieved using this mode. This value is ~10^{11} times and ~4000 times higher than a conventional QCM device, and a standard SAW device with a frequency of 978 MHz, respectively.

ACKNOWLEDGMENTS

This study was supported by the National Science Foundation of China (NSFC No.52075162), The Program of New and High-tech Industry of Hunan Province (2020GK2015, 2021GK4014), The Excellent Youth Fund of Hunan Province (2021JJ20018), Joint fund of the Ministry of Education (Young talents), the Key Research Project of Guangdong Province (2020B0101040002), the Natural Science Foundation of Changsha (kq2007026), Tianjin Enterprise Science and Technology Commissioner Project (Grant No. 19JCTPJC56200), and the Engineering Physics and Science Research Council of UK (EPSRC EP/P018998/1) and International Exchange Grant (IEC/NSFC/201078) through Royal Society and the NSFC.

Reference

[1] Collins DJ, Morahan B, Garcia-Bustos J, Doerig C, Plebanski M, Neild A. Two-dimensional single-cell patterning with one cell per well driven by surface acoustic waves. Nat Commun 2015;6:8686. DOI: 10.1038/ncomms9686

[2] Hernandez-Minguez A, Moller M, Breuer S, et al. Acoustically driven photon antibunching in nanowires. Nano Lett 2012;12(1):252-258. https://doi.org/10.1021/nl203461m

[3] Hackett L, Miller M, Brimigion F, et al. Towards single-chip radiofrequency signal processing via acoustoelectric electron-phonon interactions. Nat Commun 2021;12(1):2769. https://doi.org/10.1038/s41467-021-22935-1

[4] Tao R, McHale G, Reboud J, et al. Hierarchical Nanotexturing Enables Acoustofluidics on Slippery yet Sticky, Flexible Surfaces. Nano Lett 2020;20(5):3263-3270. https://dx.doi.org/10.1021/acs.nanolett.0c00005

[5] Wenzel SW, White RM. Analytic comparison of the sensitivities of bulk-wave, surface-wave, and flexural plate-wave ultrasonic gravimetric sensors. Applied Physics Letters 1989;54(20):1976-1978. https://doi.org/10.1063/1.101189

[6] Satzinger KJ, Zhong YP, Chang HS, et al. Quantum control of surface acoustic-wave phonons. Nature 2018;563(7733):661-665. https://doi.org/10.1038/s41586-018-0719-5

[7] Munk D, Katzman M, Hen M, et al. Surface acoustic wave photonic devices in silicon on

insulator. Nat Commun 2019;10(1):4214. https://doi.org/10.1038/s41467-019-12157-x
[8] Chen Y, Shu Z, Zhang S, et al. Sub-10 nm fabrication: methods and applications. International Journal of Extreme Manufacturing 2021;3(3). https://doi.org/10.1088/2631-7990/ac087c
[9] Büyükköse S, Vratzov B, Ataç D, van der Veen J, Santos PV, van der Wiel WG. Ultrahigh-frequency surface acoustic wave transducers on ZnO/SiO2/Si using nanoimprint lithography. Nanotechnology 2012;23(31). http://iopscience.iop.org/0957-4484/23/31/315303
[10] Mohammad MA, Chen X, Xie QY, et al. Super High Frequency Lithium Niobate Surface Acoustic Wave Transducers up to 14 GHz. 2015 Ieee International Electron Devices Meeting (Iedm). 2015. DOI: 10.1109/IEDM.2015.7409729
[11] Zheng J, Zhou J, Zeng P, et al. 30 GHz surface acoustic wave transducers with extremely high mass sensitivity. Applied Physics Letters 2020;116(12). https://doi.org/10.1063/1.5142673
[12] Fu S, Wang W, Qian L, et al. High-Frequency Surface Acoustic Wave Devices Based on ZnO/SiC Layered Structure. IEEE Electron Device Letters 2019;40(1):103-106. DOI: 10.1109/LED.2018.2881467
[13] Hashimoto KY, Sato S, Teshigahara A, Nakamura T, Kano K. High-performance surface acoustic wave resonators in the 1 to 3 GHz range using a ScAlN/6H-SiC structure. IEEE Trans Ultrason Ferroelectr Freq Control 2013;60(3):637-642. DOI：10.1109/TUFFC.2013.2606
[14] Luo JT, Zeng F, Pan F, et al. Filtering performance improvement in V-doped ZnO/diamond surface acoustic wave filters. Applied Surface Science 2010;256(10):3081-3085. DOI:10.1016/j.apsusc.2009.11.077
[15] Rodriguez-Madrid JG, Iriarte GF, Pedros J, Williams OA, Brink D, Calle F. Super-High-Frequency SAW Resonators on AlN/Diamond. IEEE Electron Device Letters 2012;33(4):495-497. DOI：10.1109/LED.2012.2183851
[16] Zhou C, Yang Y, Jin H, et al. Surface acoustic wave resonators based on (002)AlN/Pt/diamond/silicon layered structure. Thin Solid Films 2013;548:425-428. http://dx.doi.org/10.1016/j.tsf.2013.09.050
[17] Wang L, Chen S, Zhang J, et al. High performance 33.7 GHz surface acoustic wave nanotransducers based on AlScN/diamond/Si layered structures. Applied Physics Letters 2018;113(9). https://doi.org/10.1063/1.5046113
[18] Wang L, Chen S, Zhang J, et al. Enhanced performance of 17.7 GHz SAW devices based on AlN/diamond/Si layered structure with embedded nanotransducer. Applied Physics Letters 2017;111(25). https://doi.org/10.1063/1.5006884
[19] Zhou HY, Zhang SB, Li ZX, et al. Surface Wave and Lamb Wave Acoustic Devices on Heterogenous Substrate for 5G Front-Ends. 2020 Ieee International Electron Devices Meeting (Iedm). 2020. DOI: 10.1109/IEDM13553.2020.9372128
[20] Shen J, Fu S, Su R, et al. High-Performance Surface Acoustic Wave Devices Using LiNbO3/SiO2/SiC Multilayered Substrates. IEEE Transactions on Microwave Theory and Techniques 2021;69(8):3693-3705. DOI：10.1109/TMTT.2021.3077261
[21] K. Kamitani, M. Grimsditch, J. C. Nipko, C.-K. Loong, e MO. The elastic constants of silicon carbide: A Brillouin-scattering study of 4H and 6H SiC single crystals. Journal of

Applied Physics 1997;82. http://dx.doi.org/10.1063/1.366100
[22] Cimalla V, Pezoldt J, Ambacher O. Group III nitride and SiC based MEMS and NEMS: materials properties, technology and applications. Journal of Physics D: Applied Physics DOI：10.1088/0022-3727/40/20/S19
[23] Chen Z, Zhou J, Tang H, et al. Ultrahigh-Frequency Surface Acoustic Wave Sensors with Giant Mass-Loading Effects on Electrodes. ACS Sens 2020;5(6):1657-1664. DOI: 10.1021/acssensors.0c00259
[24] Solal M, Lardat R, Plessky VP, Makkonen T, Salomaa MM. Existence of harmonic metal thickness mode propagation for longitudinal leaky waves. 2004 Ieee Ultrasonics Symposium, Vols 1-3. 2004:1207-1212.
[25] Ma J, Qian L-r, Wang Y-y, et al. Theorectical Investigation Of Longitudinal Surface Acoustic Waves In Rotated Y-Cut Linbo3/Sic Heterostructures. 2020 15th Symposium on Piezoelectrcity, Acoustic Waves and Device Applications (SPAWDA); 2021:570-574. DOI: 10.1109/SPAWDA51471.2021.9445477
[26] Kaletta UC, Wenger C. FEM simulation of Rayleigh waves for CMOS compatible SAW devices based on AlN/SiO(2)/Si(100). Ultrasonics 2014;54(1):291-295. http://dx.doi.org/10.1016/j.ultras.2013.04.009
[27] Takagaki Y, Santos PV, Wiebicke E, Brandt O, Schönherr HP, Ploog KH. Guided propagation of surface acoustic waves in AlN and GaN films grown on 4H–SiC(0001)substrates. Physical Review B 2002;66(15). DOI: 10.1103/PhysRevB.66.155439
[28] Feld DA, Parker R, Ruby R, Bradley P, Dong S. After 60 years: A new formula for computing quality factor is warranted. 2008 IEEE Ultrasonics Symposium; 2008:431-436. DOI: 10.1109/ULTSYM.2008.0105.
[29] Thomas S, Cole M, Villa-López FH, Gardner JW. High frequency surface acoustic wave resonator-based sensor for particulate matter detection. Sensors and Actuators A: Physical 2016;244:138-145. http://dx.doi.org/doi:10.1016/j.sna.2016.04.003
[30] Kadota M, Yoneda T, Fujimoto K, Nakao T, Takata E. Resonator filters using shear horizontal-type leaky surface acoustic wave consisting of heavy-metal electrode and quartz substrate. Ieee Transactions on Ultrasonics Ferroelectrics and Frequency Control 2004;51(2):202-210. DOI：10.1109/tuffc.2004.1295395
[31] Hsu-Cheng O, Zaghloul M. Synchronous One-Pole LiNbO3 Surface Acoustic Wave Mass Sensors. IEEE Electron Device Letters 2010;31(5):518-520. DOI：10.1109/LED.2010.2043636
[32] Ten ST, Hashim U, Gopinath SCB, et al. Highly sensitive Escherichia coli shear horizontal surface acoustic wave biosensor with silicon dioxide nanostructures. Biosens Bioelectron 2017;93:146-154. http://dx.doi.org/10.1016/j.bios.2016.09.035
[33] Kuo FY, Wei HL, Yao DJ. PM2.5 Detection by Cyclone Separator Combined with SH-SAW Sensor. 2017 Ieee 12th International Conference on Nano/Micro Engineered and Molecular Systems (Nems). 2017:248-251. DOI: 10.1109/NEMS.2017.8017017.
[34] Ma W, Tang S, Wei Y, Xie G. Simple biosensing method to detect DMMP based on QCM transducer and acetylcholine esterase sensitive film. Micro & Nano Letters 2017;12(2):113-116. DOI: 10.1049/mnl.2016.0497
[35] Huang XH, Pan W, Hu JG, Bai QS. The Exploration and Confirmation of the Maximum Mass Sensitivity of Quartz Crystal Microbalance. IEEE Trans Ultrason Ferroelectr Freq

Control 2018;65(10):1888-1892. DOI: 10.1109/TUFFC.2018.2860597
[36] Pan W, Huang X, Chen Q. Uniformization of Mass Sensitivity Distribution of Silver Electrode QCM. IEEE Trans Ultrason Ferroelectr Freq Control 2020;67(9):1953-1956. DOI：10.1109/TUFFC.2020.3008790